Periodic chaotic billiards: Quantum-classical correspondence in energy space

G. A. Luna-Acosta, J. A. Méndez-Bermúdez, and F. M. Izrailev
Instituto de Física, Universidad Autónoma de Puebla, Apartado Postal J-48, Puebla 72570, Mexico
(Received 13 April 2001; published 20 August 2001)

We investigate the properties of eigenstates and local density of states (LDOS) for a periodic two-dimensional rippled billiard, focusing on their quantum-classical correspondence in energy representation. To construct the classical counterparts of LDOS and the structure of eigenstates (SES), the effects of the boundary are first incorporated (via a canonical transformation) into an effective potential, rendering the one-particle motion in the 2D rippled billiard equivalent to that of two interacting particles in 1D geometry. We show that classical counterparts of SES and LDOS in the case of strong chaotic motion reveal quite a good correspondence with the quantum quantities. We also show that the main features of the SES and LDOS can be explained in terms of the underlying classical dynamics, in particular, of certain periodic orbits. On the other hand, statistical properties of eigenstates and LDOS turn out to be different from those prescribed by random matrix theory. We discuss the quantum effects responsible for the nonergodic character of the eigenstates and individual LDOS that seem to be generic for this type of billiards with a large number of transverse channels.

DOI: 10.1103/PhysRevE.64.036206 PACS number(s): 05.45.−a, 45.05.+x

I. INTRODUCTION

The goal of this study is to deepen our understanding of the quantum-classical correspondence for chaotic systems by analyzing the properties of eigenstates and local density of states (LDOS) in the energy representation. This approach has already been successfully applied to models of two interacting particles [1–3] and to a three orbital schematic shell model [4]. In this paper we extend this approach to chaotic periodic billiards by incorporating the effects of the boundaries into the Hamiltonian operator and treating the degrees of freedom as independent ''particles.'' Some results of this work were advanced in [5].

The outline of the paper is as follows. Section II presents some basic features of the classical dynamics of the rippled billiard, together with the necessary details of its quantum description. In Sec. III the classical representation of the model is given. In Sec. IV we discuss the meaning of the structure of eigenstates (SES) and LDOS, and in Secs. V and VII we define their classical counterparts. In Sec. VII we compare the quantum and classical SES and LDOS. Section VIII pertains to the individual properties of eigenstates and LDOS. In Sec. IX we make some concluding remarks.

II. DESCRIPTION OF THE MODEL

The system that we shall use to explore the quantum-classical correspondence is a two-dimensional (2D) billiard with periodic boundary conditions along the longitudinal coordinate x. The top profile is given by the function $y=d+a\xi(x)$ with $\xi(x+2\pi)=\xi(x)$, where a is the amplitude of the ripple and d is the width of the billiard when a is zero. The bottom boundary is flat (see Fig. 1).

The first studies of the classical dynamics of this system were performed in Ref. [6] in connection with the beam-beam interaction problem (see also [7]). More recently, the finite length version of this system was analyzed in Ref. [8] as a model of a mesoscopic electron waveguide, where a transport signature of chaos in the behavior of resistivity was established. The same model has been also used [9] to study certain *quantum* transport properties through ballistic cavities. On the other hand, the analysis of the band-energy spectrum for an *infinitely* long rippled channel [10] in the cases of mixed and global classical chaos provides insight into the universal features of electronic band structures of real crystals [11]. In Ref. [12] a similar periodic billiard was considered in connection with the problem of chaotic diffusion in the systems with band spectra, see also Refs. [13,14].

An attractive feature of this rippled channel is that its classical phase space undergoes the generic transition to global chaos as the ripple amplitude a increases. Hence results obtained for this particular system are expected to be applicable to a large class of systems, namely, nondegenerate, nonintegrable Hamiltonians.

In the quantum description the model is given by the Hamiltonian

$$\hat{H}=\frac{1}{2m_e}(\hat{P}_x^2+\hat{P}_y^2)=-\frac{\hbar^2}{2m_e}(\partial_x^2+\partial_y^2) \tag{1}$$

for the wave function $\Psi(x,y)$ obeying the boundary conditions $\Psi(x,y)=0$ at $y=0$ and $d+a\xi(x)$. There exist various numerical methods that can be used to obtain the eigenvalues and eigenfunctions of nonintegrable billiards, such as the transfer matrix approach [15], the scaling method [16], and the scattering approach [12]. Here we shall employ a different technique that is tailored to explore the quantum-classical correspondence of the structure of eigenstates. It

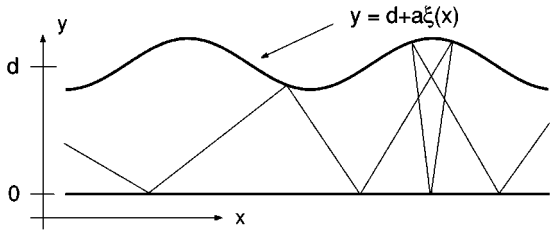

FIG. 1. Geometry of a rippled billiard.

consists of representing the Hamiltonian (1) in new coordinates (u,v) in such a way that the effects of the boundary are transferred to an effective interaction potential between the two degrees of freedom (u,v). That is, the coordinates (u,v) are chosen so that the new wave function satisfies ''flat'' boundary conditions: $\Psi(u,v)=0$ at $v=0,d$. For our rippled channel, this can be accomplished by the transformation

$$u=x,$$

$$v=\frac{yd}{d+a\xi(x)}=\frac{y}{1+\epsilon\xi(x)}, \tag{2}$$

where $\epsilon\equiv a/d$ is a measure of the perturbation due to the ripple [17]. The Schrödinger equation in the new coordinates can be obtained from the covariant expression for a particle moving (in the absence of potentials) in a Riemannian curved space [18],

$$-\frac{\hbar^2}{2m_e}\Delta_{\rm cov}\Psi(u,v)=\frac{\hbar^2}{2m_e}g^{-1/2}\partial_\alpha g^{\alpha\beta}g^{1/2}\partial_\beta\Psi(u,v). \tag{3}$$

Here $\Delta_{\rm cov}$ is the Laplace-Beltrami operator, g is the metric and $g^{\alpha\beta}$ is the metric tensor. Even though Eq. (3) is still the kinetic energy, the resulting differential equation takes a much more complicated form than the ordinary Laplacian. This is the price we have to pay when we transfer the effect of the boundaries onto the operator [the explicit form of the Schrödinger equation in (u,v) coordinates for the rippled billiard is given in [10]]. Moreover, the coordinate representation of the canonical momentum has now the form [19]

$$\hat{P}_\alpha=-i\hbar[\partial_\alpha+\tfrac{1}{4}\partial_\alpha\ln(g)]=-i\hbar g^{-1/4}\partial_\alpha g^{1/4}. \tag{4}$$

Substitution of this expression into the Schrödinger equation (3) determines the quantum Hamiltonian in covariant form [19],

$$\hat{H}=\frac{1}{2m_e}g^{-1/4}\hat{P}_\alpha g^{\alpha\beta}g^{1/2}\hat{P}_\beta g^{-1/4}\quad \alpha,\beta=u,v. \tag{5}$$

Substituting now the explicit expressions for the metric tensor $g^{\alpha\beta}$ and metric g,

$$g^{\alpha\beta}=\begin{pmatrix} 1 & \dfrac{-\epsilon v\xi_u}{1+\epsilon\xi} \\ \dfrac{-\epsilon v\xi_u}{1+\epsilon\xi} & \dfrac{1+\epsilon^2v^2\xi_u^2}{(1+\epsilon\xi)^2}\end{pmatrix}, \tag{6}$$

$$g=\mathrm{Det}(g_{\alpha\beta})=[1+\epsilon\xi u]^2, \tag{7}$$

we get

$$\hat{H}=\frac{1}{2m_e}g^{-1/4}\Big\{\hat{P}_u(1+\epsilon\xi)\hat{P}_u+\hat{P}_v\frac{1+\epsilon^2v^2\xi_u^2}{1+\epsilon\xi}\hat{P}_v - \epsilon[\hat{P}_u v\xi_u\hat{P}_v+\hat{P}_v v\xi_u\hat{P}_u]\Big\}g^{1/4}, \tag{8}$$

where $\xi_u=d\xi/du$. Note that the effects of the rippled boundary are fully incorporated into the Hamiltonian operator. Since the boundary conditions in the new coordinates correspond to those of a ''flat'' channel, $\Psi(u,v)=0$ at $v=0,d$. For our purposes it is convenient now to separate the Hamiltonian (8) as

$$\hat{H}=\hat{H}^0+\hat{V}(u,v,\hat{P}_u,\hat{P}_v), \tag{9}$$

where

$$\hat{H}^0=\frac{1}{2m_e}(\hat{P}_u^2+\hat{P}_v^2) \tag{10}$$

with [cf. Eqs. (4) and (7)]

$$\hat{P}_u=-i\hbar\left[\partial_u+\frac{1}{4}\partial_u\ln(g)\right],\quad \hat{P}_v=i\hbar\partial_v, \tag{11}$$

and $\hat{V}$ stands for the rest of the terms.

We remark that this representation allows us to treat the original model of one free particle in the rippled channel as a 1D model of two interacting ''particles'' identified with the two degrees of freedom u and v. Here H^0 is the Hamiltonian of two *noninteracting particles*. The eigenfunctions of H^0 define the unperturbed basis in which the eigenstates of the total Hamiltonian $\hat{H}(u,v,\hat{P}_u,\hat{P}_v)$ may be expanded. Such a representation turns out to be convenient for the study of chaotic properties of the model since one can use the tools and concepts developed in the theory of interacting particles (see, for example, [20]).

Since the Hamiltonian (8) is periodic in u, the eigenstates are Bloch states. This allows us to write the solution of the Schrödinger equation in the form $\Psi_E(u,v)=\exp(iku)\Phi_k(u,v)$ with $\Phi_k(u+2\pi,v)=\Phi_k(u,v)$. For an infinite periodic channel the Bloch wave vector $k=k(E)$ takes a continuous range of values, which we take to lie in the first Brillouin zone $(-\frac{1}{2}\leqslant k\leqslant\frac{1}{2})$.

By expanding $\Phi_k(u,v)$ in a double Fourier series the αth eigenstate of energy $E^\alpha(k)$ can be written as

$$\Psi^\alpha(u,v;k)=\sum_{m=1}^{\infty}\sum_{n=-\infty}^{\infty}C_{mn}^\alpha(k)\phi_{mn}^k(u,v), \tag{12}$$

where

$$\phi_{mn}^k(u,v)=\langle u,v|m,n\rangle_k =\pi^{-1/2}g^{-1/4}\sin(m\pi v/d)\exp[i(k+n)u] \tag{13}$$

are the eigenstates of the unperturbed Hamiltonian $\hat{H}^0(u,v)$ with corresponding eigenvalues

$$E_{n,m}^{(0)}(k)=\frac{\hbar^2}{2m_e}\left[(k+n)^2+\left(\frac{m\pi}{d}\right)^2\right]. \tag{14}$$

The factor $\pi^{-1/2}g^{-1/4}$ in Eq. (13) appears from the orthonormality condition in the curvilinear coordinates (u,v). Thus, the exact eigenstates are expanded in a complete orthonor-

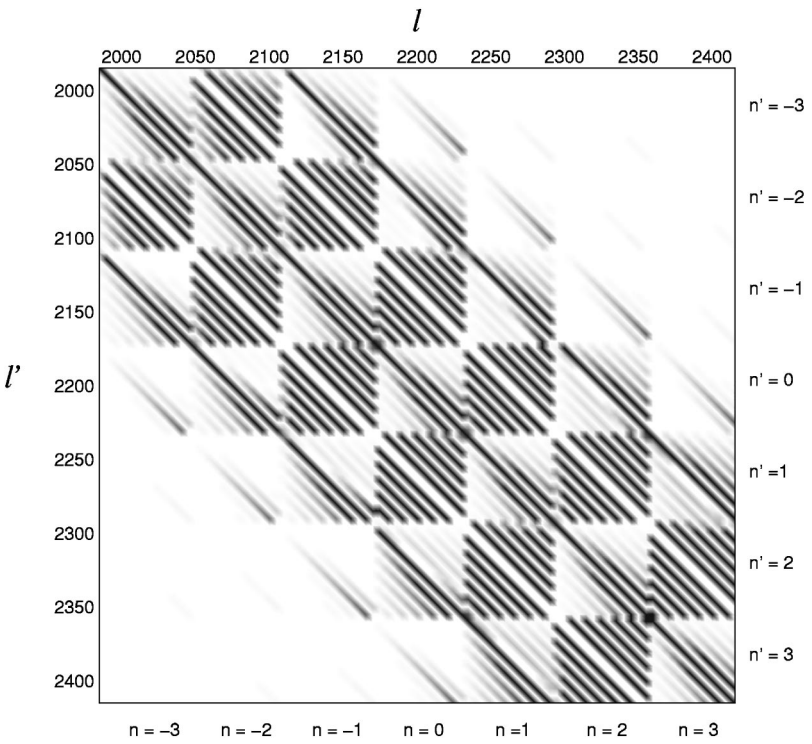

FIG. 2. Central part of the 4030×4030 Hamiltonian matrix $H_{l,l'}(k)$: $N_{\max}=32$ and $M_{\max}=62$. The 62×62 blocks corresponding to $n, n'=0, \pm1, \pm2, \pm3$ are shown.

mal basis satisfying the boundary conditions of the problem, i.e., a Galerkin series expansion [21].

So far, there has been no need to specify the ripple function $\xi(x)$, except that it is periodic: $\xi(x+2\pi)=\xi(x)$. For concreteness, we consider from now on the dependence $\xi(x)=\cos(x)$. The ripple profile is given by $y=d+a\cos(x)$ where x, y, d, and a are dimensionless quantities. The latter are defined from the expression $Y=D+A\cos(2\pi X/B)$ scaled to the period B. Therefore, $x=2\pi X/B$, $y=2\pi Y/B$, $d=2\pi D/B$, and $a=2\pi A/B$, where X, Y, D, A, and B are dimensional quantities.

This approach to solving the Schrödinger equation was used to calculate the energy-band structure and Husimi distributions of the rippled channel [10], and to obtain the energy level statistics under the conditions of full and mixed chaos [22]. Specifically, in Ref. [22] the energy level spacing distribution was shown to be Poisson, Wigner-Dyson, or intermediate between these two, for regular, globally chaotic, or mixed classical motion, respectively, in agreement with the well-known RMT conjecture [23]. Most relevant to our work here is the fact that these distributions were found to be the same for all values of k within the Brillouin zone, except $k\approx0$ for which the parity symmetry should be taken into account. Thus, without loss of generality we fix the value $k=0.1$. We shall also use in all our calculations the following values for the amplitude a and width d of the rippled channel: $a/2\pi=0.06$ and $d/2\pi=1.0$. These values produce representative global chaotic motion in the classical limit (see below).

In order to study the structure of eigenstates of the total Hamiltonian $\hat{H}(u,v)$ one needs, first, to choose a way of ordering the unperturbed basis in which to represent the Hamiltonian matrix $H_{l,l'}(k)=\langle l|\hat{H}|l'\rangle_k$. Specifically, we have to assign an index l, labeling the basis state $|l\rangle_k \equiv|m,n\rangle_k$, to each pair of indicies (m, n) (note that, although the energy spectra is independent of the assignment $(m,n)\rightarrow l$, the structure of the eigenstates is not). The size of the Hamiltonian matrix is determined by the maximum values of n and m: $-N_{\max}\leqslant n\leqslant N_{\max}$ and $1\leqslant m\leqslant M_{\max}$.

A natural assignment is the following one. Let us fix the lowest value of n $(-N_{\max})$ and sweep all values of m $(1\leqslant m\leqslant M_{\max})$. This gives $l=1,2,\ldots,M_{\max}$. Then do the same for $n=-N_{\max}+1$, which gives $M_{\max}+1\leqslant l\leqslant 2M_{\max}$ and so on, till finally we have $1\leqslant l\leqslant L_{\max}$, where $L_{\max}=(2N_{\max}+1)M_{\max}$ defines the matrix size, $L_{\max}\times L_{\max}$. This rule results in a block structure of the Hamiltonian matrix, with block size equal to $M_{\max}$. Figure 2 shows the central part of a 4030×4030 matrix with $(N_{\max},M_{\max})=(32,62)$. Here we can see a number of blocks of size 62×62 corresponding to $n,n'=0,\pm1,\pm2,\pm3$. In this representation the matrix is clearly a band matrix. The finite size of the band is due to the short range coupling between different blocks, namely, the strength of the matrix elements decrease as $\epsilon^{|n-n'|}$, $\epsilon^{|n-n'\pm1|}$, or $\epsilon^{|n-n'\pm2|}$ (see details in [10]).

The above way of ordering the unperturbed basis is typical; it corresponds to the ''channel representation'' since the index m labels a specific transverse channel (or mode) for the propagation of the wave through the billiard, see Eq. (13). However, for our purposes it is essential to use the ''energy representation,'' according to which the unperturbed basis is ordered in increasing energy, $E^0_{l+1}(k)\geqslant E^0_l(k)$. This defines a new rule $l\rightarrow l_{\text{new}}=l_{\text{new}}(n,m)$. Figure 3 shows the difference between these two ways of ordering of the basis, giving the normalized unperturbed energy $\overline{E^0_l}(k)\equiv E^0_l(k)/E^*=(d/\pi)^2(n+k)^2+m^2$ with $E^*\equiv(\hbar^2/2m_e)(\pi^2/d^2)$, as a function of l.

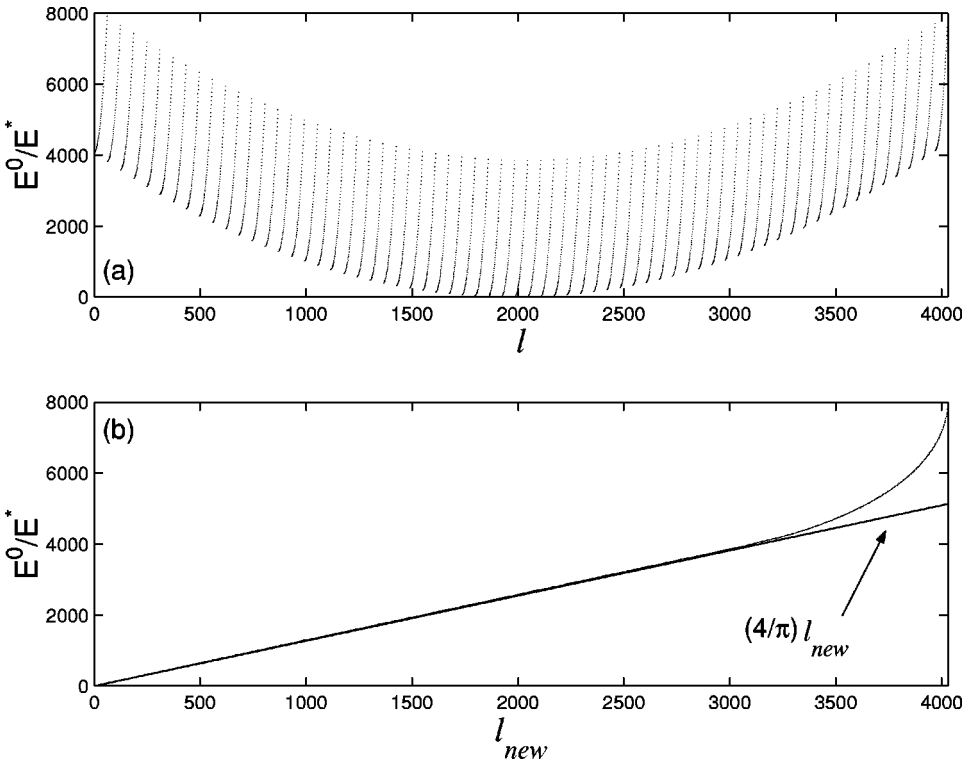

FIG. 3. (a) Unperturbed energy spectra as a function of l. (b) Unperturbed energy spectra ordered in energy as a function of l_{new}.

A nonmonotonic dependence of the energy occurs in Fig. 3(a) because the first rule $l(m,n)$ described above produces minimum values in the energy for $m=1$. In contrast, in Fig. 3(b) a linear dependence of the unperturbed energy on the index l_{new} is shown, apart from large values of l_{new} where the finiteness of the matrix results in the distortion of the spectra. The numerical obtained linear dependence, $\overline{E}\equiv E/E^*=(4/\pi)l_{\mathrm{new}}$, can be derived analytically from Weyl's formula $\overline{N}(E)=SEm_a/2\pi\hbar^2$, valid for 2D billiards with area S (also valid for periodic 2D billiards) [24].

A crucial point is that the eigenstates of the total Hamiltonian in the ''energy representation'' have a very convenient form for the analysis. The advantage of the ''energy representation'' is clearly seen in Fig. 4 where an arbitrarily cho-

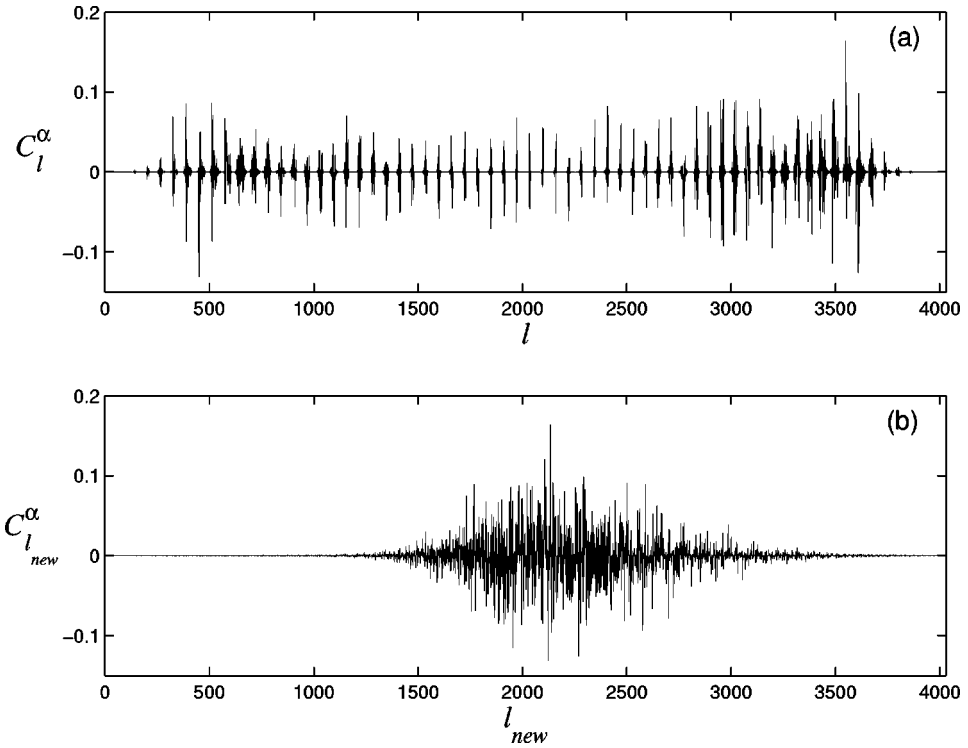

FIG. 4. Example of eigenfunctions for different ways of ordering the unperturbed basis. (a) The state $\alpha=2122$ as a function of l, (b) the same state as a function of l_{new}.

sen eigenstate is given in the two representations. One can see that in one case the eigenstate has a kind of regular and extended structure, while in the other, the eigenstate is compressed around the unperturbed state whose energy is close to the energy of the perturbed state. In the latter case one may use a statistical approach to describe the global properties of such eigenstates, see Refs. [20,25,26]. Specifically, we may characterize such eigenstates by introducing an envelope around which the components are expected to fluctuate in a pseudorandom way. We stress that by using this energy ordering one can relate the global form of eigenstates in the energy representation with its classical counterpart, see below.

III. CLASSICAL REPRESENTATION OF THE MODEL

Clearly, the type of motion of a particle in the ripple billiard depends on the values of the geometrical parameters, namely, on the ripple amplitude a and the average width d. If the channel is narrow, $d \ll 2\pi$, the Poincaré section reveals a large resonance island surrounded by the typical Poincaré-Birkhoff structure [6,8,10]. This island is formed by the librational motion along the x direction in the neighborhood of $x=0$. On the contrary, for wide channels ($d \geqslant 2\pi$) global chaos occurs even for small amplitudes due to a strong overlap of resonances. In this work we shall limit ourselves to the study of global chaos, i.e., wide channels.

The condition of global chaos can be derived analytically for the case of small amplitude $a \ll d$ where the following approximate map is valid [27],

$$\begin{aligned} \alpha_{n+1} &= \alpha_n + 2a \sin(x_n), \\ x_{n+1} &= x_n + 2d \cot(\alpha_{n+1}) \pmod{2\pi}. \end{aligned} \tag{15}$$

Here x_n is the position of a particle and α_n is the angle between the x axis and the velocity of the particle, right after the nth collision with the upper wall. The standard linearization around fixed points of period one yields

$$\begin{aligned} \delta\alpha_{n+1} &= \delta\alpha_n + \kappa \sin(\Delta x_n), \\ \Delta x_{n+1} &= \Delta x_n + \delta\alpha_{n+1} \pmod{2\pi}, \quad \kappa \equiv 2da/\pi, \end{aligned} \tag{16}$$

where the angle $\delta\alpha$ and the position Δx, measured from the fixed point, play the role of the action and angle variables, respectively. Equation (16) has the form of the *standard map* with κ as the nonlinear parameter. Hence, Chirikov's overlapping criteria predicts the onset of global chaos for $\kappa \simeq 1$. This was confirmed by computing numerically the actual path of the particle as it travels along the channel. Specifically, for $\kappa \geqslant 1$ the Poincaré section (α_n, x_n) shows global chaos for wide channels. In this paper we shall consider a wide channel with small ripple amplitude, specified by the parameters $(a/2\pi, d/2\pi) = (0.06, 1.0)$, therefore, $\kappa \approx 1.5$.

Let us now write, as in the quantum description, the classical Hamiltonian in the (u,v) coordinates so that the effects of the rippled boundary can be incorporated as a kind of coupling between two degrees of freedom. The classical Hamiltonian is

$$H = \frac{1}{2m_e} g^{\alpha\beta} P_\alpha P_\beta, \tag{17}$$

which can be obtained from the quantum Hamiltonian (8) by commuting all momenta and coordinates [28].

For completeness, the canonical transformation between (x,y,P_x,P_y) and (u,v,P_u,P_v) are given by Eq. (2) together with $P_u = P_x + yP_y/(1+\epsilon\xi)$ and $P_v = (1+\epsilon\xi)P_y$. Inserting the metric tensor equation (6) into Eq. (17) and regrouping terms, the Hamiltonian can be written as $H = H^0 + V$, where

$$H^0 = \frac{1}{2m_e}(P_u^2 + P_v^2) \tag{18}$$

and

$$V = -\frac{1}{2m_e}\epsilon\left[\frac{2\xi + \epsilon(\xi^2 + v^2\xi_u^2)}{(1+\epsilon\xi)^2} P_v^2 + \frac{2\xi_u}{1+\epsilon\xi} P_u P_v\right]. \tag{19}$$

V represents the interaction between the two "particles" u and v (here $\xi_u = d\xi/du$ and $\epsilon = a/d$).

IV. STRUCTURE OF EIGENSTATES AND LDOS: DEFINITIONS

Once the matrix $H_{l,l'}(k)$ has been diagonalized, its eigenstates $\Psi^\alpha(k) = \Sigma C_l^\alpha(k)\phi_l^k$ are also reordered in energy: $E^{\alpha+1} \geqslant E^\alpha$. We adopt the convention that the greek superindex (latin subindex) denotes the exact (unperturbed) state. The amplitudes $C_l^\alpha(k)$ from the "state vector matrix." The elements along the row α of this matrix are the components of the αth eigenstate in the representation of the unperturbed energy-ordered basis. Correspondingly, the elements along the column l give the unperturbed state l expanded in the energy-ordered perturbed basis. For our purposes, we examine the matrix $w_l^\alpha \equiv |C_l^\alpha(k)|^2$ (see Fig. 5), which plays the central role in our approach.

The rows of the matrix w_l^α show how a specific eigenfunction (eigenstate $|\alpha\rangle$) is expanded in the unperturbed basis $|l\rangle$. Since the average "bandwidth" of w_l^α smoothly depends on the index α (equivalently on the energy E^α), it is convenient to average w_l^α over a small range of eigenstates. In this way, one can obtain the so-called SES in the unperturbed basis. In what follows, we are interested in the SES in the energy representation, which is defined as [29]

$$W(E_l^0 | E^\alpha) = \sum_{\alpha'} \overline{w}_l^{\alpha'} \delta(E_l^0 - E^{\alpha'}), \tag{20}$$

where $\overline{w}_l^{\alpha'} = w_l^{\alpha'}/N$ with N as the number of eigenstates $|\alpha'\rangle$ in the vicinity of a given α. The structure of eigenstates $W(E_l^0|E^\alpha)$ gives the dependence on the unperturbed energy E_l^0 for eigenstates with total energy close to E^α. This sum can be approximated by an integral that involves the density of states $\rho(E^\alpha)$ providing the transition from the basis to the energy representation. This function SES plays the key role in the determination of important physical quantities, such as

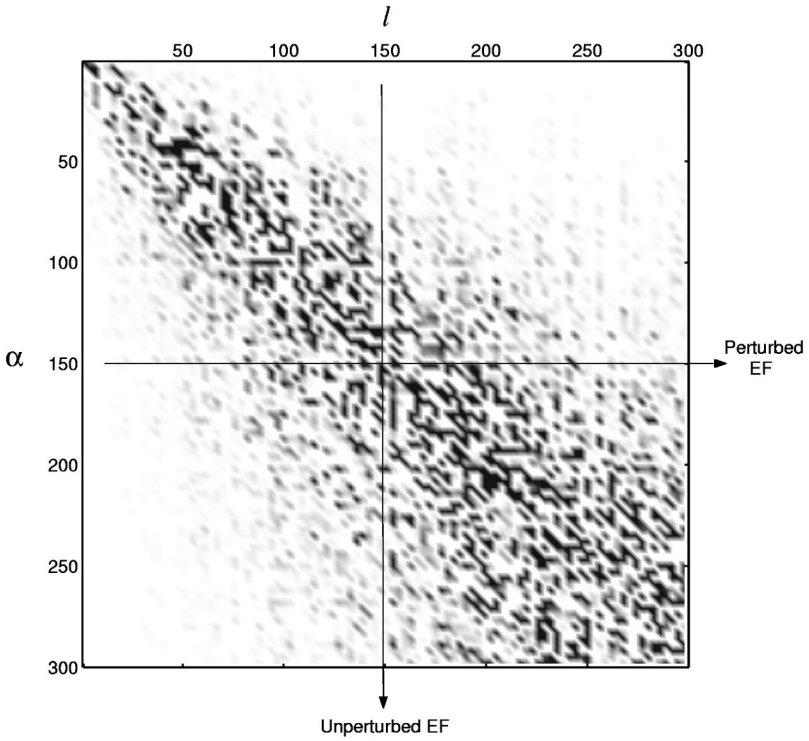

FIG. 5. Left upper part of the matrix w_l^α corresponding to $N_{\max}=32$ and $M_{\max}=62$.

the distribution of occupation numbers in chaotic closed systems (see, for example, [2,20,30]).

Analogously, one can analyze the columns of the matrix w_l^α, which give information about a given *unperturbed* state $|l\rangle$ spanned over *exact* eigenstates $|\alpha\rangle$. Therefore, one can define the following quantity

$$\omega(E^\alpha|E_l^0)=\sum_{l'} \overline{w}_{l'}^{\alpha}\,\delta(E^\alpha-E_{l'}^0), \tag{21}$$

which is well known in nuclear physics as the *strength function*, and in solid state physics as the LDOS. In Eq. (21) the summation (average) is done over *N basis* states $|l'\rangle$ around a fixed state $|l\rangle$, $\overline{w}_{l'}^{\alpha}=w_{l'}^{\alpha}/N$. Therefore, this quantity is considered as a function of the energy E^α. It shows how a given unperturbed state $|\phi_l\rangle$ is coupled to the exact states due to the interaction V. The width of this function (*spreading width*) determines the energy range associated with the "decay" of a given unperturbed state into other states when the interaction is switched on.

V. CLASSICAL ANALOG OF THE STRUCTURE OF EIGENFUNCTIONS

An essential point is that both the structure of eigenstates and the local density of states have well-defined classical analogs [29]. Let us first start with the SES. Since $C_l^\alpha=\langle\Psi^\alpha|\phi_l\rangle$ as a function of l is the *projection* of the perturbed state onto the states of the unperturbed system, the classical counterpart of $w_l^\alpha=|C_l^\alpha|^2$ as a function of energy E_l can be defined as the *projection* of the total Hamiltonian H onto the unperturbed one H^0, where $H=H^0+V$, where V is the perturbation [29]. This projection can be numerically done by substituting the trajectories $\Phi(t)\equiv(x(t),y(t),p_x(t),p_y(t))$ generated by the Hamiltonian H with energy E onto the unperturbed Hamiltonian H^0. Since the unperturbed energy $E^0(t)$ along these trajectories varies in time, it fills the so-called *energy shell* characterized by its width ΔE. Therefore, for chaotic total Hamiltonians H, the classical analog $W_{\rm cl}(E^0|E)$ of the quantum SES can be easily obtained from $E^0(t)$.

In Fig. 6(a) we show the energy of the unperturbed Hamiltonian H^0 as a function of time after the substitution of a single chaotic trajectory $\phi(t)$ generated by the perturbed Hamiltonian H into H^0. The classical distribution $W_{\rm cl}(E^0|E)$ [see Fig. 6(b)] is constructed from $E^0(t)$, averaged over a sufficiently long time. Alternatively, since the dynamics of H is chaotic, the same distribution can be obtained by averaging over many different orbits at a shorter time. For concreteness, in what follows we chose $E=1$.

It is important to understand the origin of the shape of the classical distribution [see Fig. 6(b)] in view of its correspondence to the quantum SES. For this, let us examine in detail characteristic time intervals of the plot of $E^0(t)$ together with plots of P_u^2, P_v^2, and v, see Figs. 7(a)–7(d). From Fig. 6(a) it is clear that the main contribution to the central peak of the distribution $W_{\rm cl}(E^0|E)$ comes from the continuous time intervals where $E^0\approx 1$. These intervals in turn correspond to $P_u^2\approx 2$ (the maximum value) and to $P_u^2\approx 0$ [see Figs. 7(b) and 7(c)]. During these time intervals the particle travels almost parallel to the x axis (u axis). In fact, from the plot of $v(t)$ [Fig. 7(d)] one can see that the particle hits only once the bottom boundary during a relatively long time. The contribution to the central peak can also be seen directly from the expressions (18) and (19). Indeed, since $P_v^2\approx 0$, we have $E^0(t)\approx\frac{1}{2}P_u^2\approx E=1$.

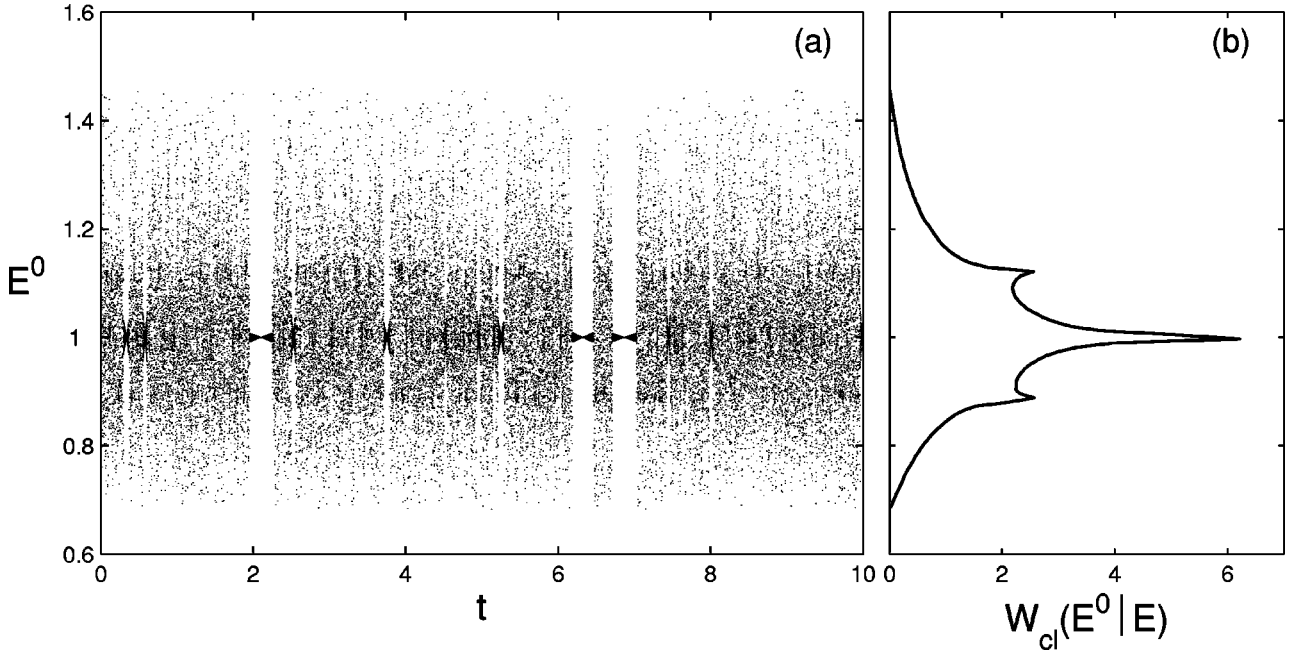

FIG. 6. (a) Energy of the unperturbed Hamiltonian $E^0(t)$ as a function of time (in arbitrary units) for $E=1$. Note the intermittent structure (from noiselike to stablelike) in $E^0(t)$. (b) Classical distribution $W_{\mathrm{cl}}(E^0|E)$ constructed from $E^0(t)$.

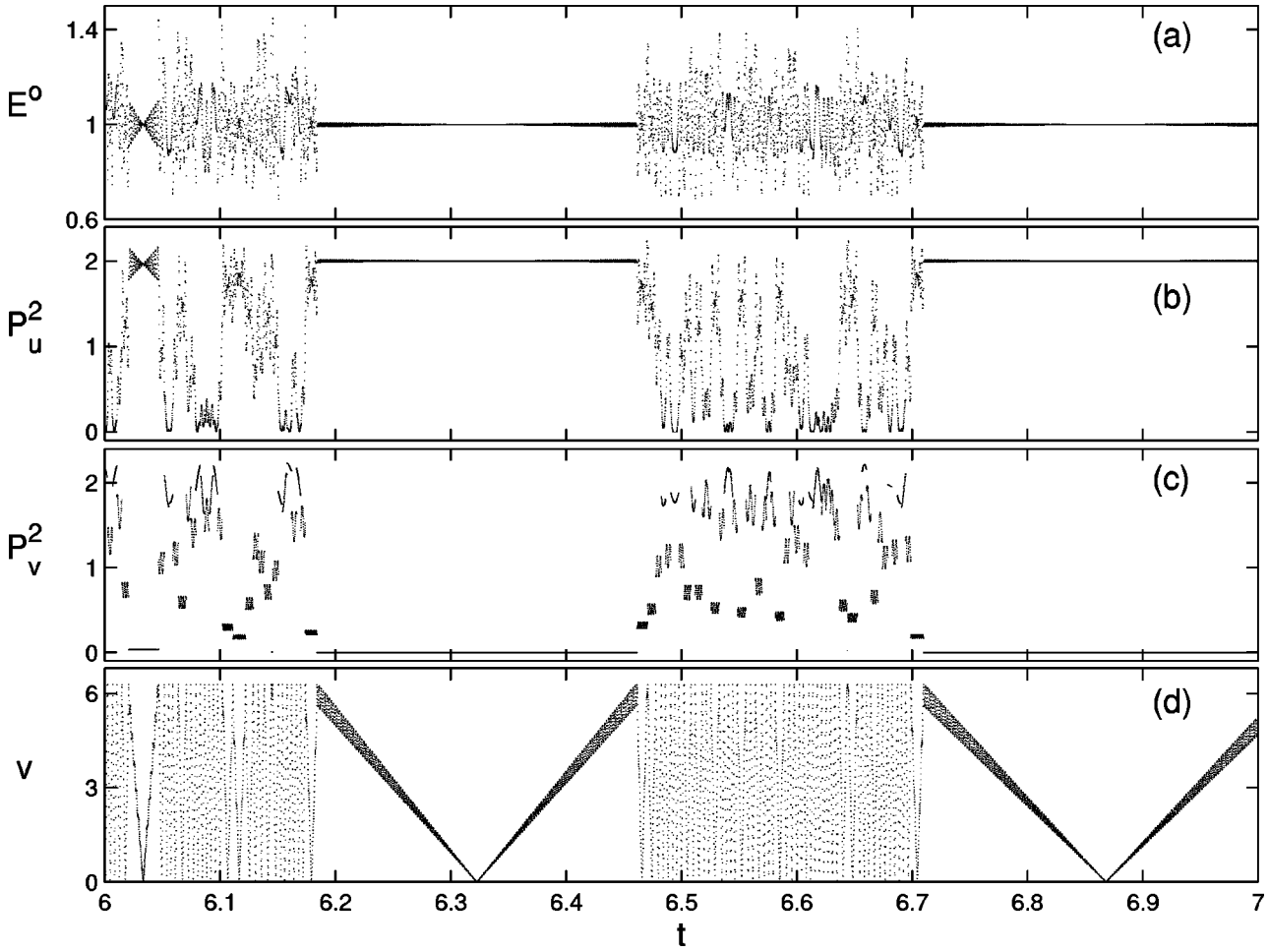

FIG. 7. Energy E^0 and P_u^2, P_v^2, v as a function of time (in arbitrary units) on a short time scale after the substitution of a trajectory $\phi(t)\in H$ onto H^0 for $E=1$.

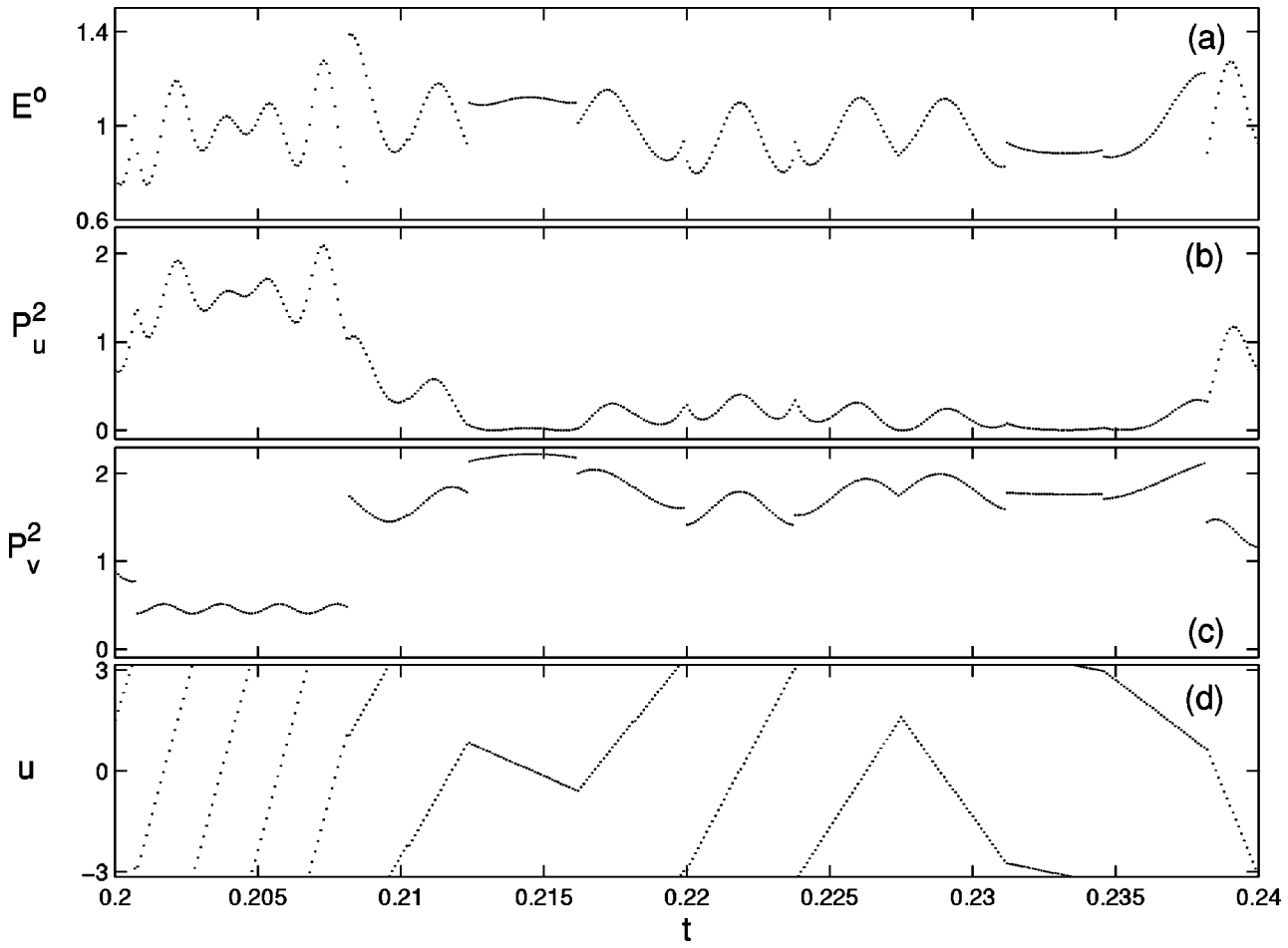

FIG. 8. The same as in Fig. 7 for a different time interval.

In the same way one can understand the origin of two side-band peaks in the form of $W_{\rm cl}(E^0|E)$, clearly seen in Fig. 6(b). The data reported in Figs. 8(a)–8(d) show that for small time intervals, e.g., $0.212<t<0.216$ and $0.231<t<0.234$ the value of E^0 is practically constant ($E^0\approx 1.12$ and $E^0\approx 0.88$, respectively). These values of E^0 correspond to the right and left peaks in Fig. 6(b). Contrary to the data in Fig. 6 explaining the origin of the central peak, in the two time regions of Fig. 8 the value of P_u^2 is nearly zero and P_v^2 is nearly maximum [see Figs. 8(b) and 8(c)]. In these regions the motion of the particle is almost perpendicular to the x axis (u axis).

The form of the profile $\xi(u)=\cos(u)$ in our ripple channel results in two periodic orbits of period 1: the stable one for $P_u=0$, $u=0$ and the unstable one for $P_u=0$, $u=\pi$. Putting these values for P_u and u into expressions (18) and (19), we find the values for P_v^2. This allows us to obtain the value of H^0 for these two periodic orbits, $E^0=E(1+\epsilon)^2\approx 1.12$ and $E^0=E(1-\epsilon)^2\approx 0.88$, respectively for $u=0$ and $u=\pi$. Thus, the left (right) peak of the distribution $W_{\rm cl}(E^0|E)$ is formed by trajectories dwelling near the unstable (stable) periodic orbits of period 1.

VI. CLASSICAL ANALOG OF THE LDOS

In analogy with the quantum LDOS, the classical LDOS distribution $\omega_{\rm cl}(E|E^0)$ is constructed by projecting the dynamics generated by $H^0=E^0$ onto the Hamiltonian $H=H^0+V$. Here, because H^0 is integrable, several (*regular*) trajectories of H^0 have to be substituted into H and then averaged in time, in contrast with the classical SES where only one (*chaotic*) trajectory over a sufficiently long time is needed to form the distribution. The result of this procedure is exemplified in Fig. 9(a) where $E(t)$ is shown for 36 regular trajectories, whose initial conditions were chosen to lie on a mesh of points distributed uniformly in the plane (P_u,u) (v is fixed and P_v is determined by the constant energy $E^0=1$). The classical LDOS distribution $\omega_{\rm cl}(E|E^0)$, see Fig. 9(b), was obtained from $E(t)$ [Fig. 9(a)].

In the construction of Fig. 9(a), six initial conditions for u (taken from the interval $[-\pi,\pi]$) were used for each of the six initial values of P_u [from the interval $(-\sqrt{2E^0},\sqrt{2E^0})$]. Hence the appearance of six similar sets formed by six small time intervals. The very first time interval ([0, 0.25]) yields $E=1$ and is produced by a trajectory with initial condition $P_u\gtrsim-\sqrt{2}$ and $u=-\pi$, i.e., a grazing trajectory. The next interval [0.25, 0.5], a bar-code-like structure extending over the whole energy shell, is produced by the initial condition $P_u=-0.6\sqrt{2}$, $u=-\pi$, and the third interval [0.5, 0.75], the noiselike one, is produced by the initial condition $P_u=-0.2\sqrt{2}$, $u=-\pi$. The next three intervals are produced by mirror initial conditions ($P_u=0.2\sqrt{2}$ $0.6\sqrt{2}$, and $\lesssim\sqrt{2}$ with u

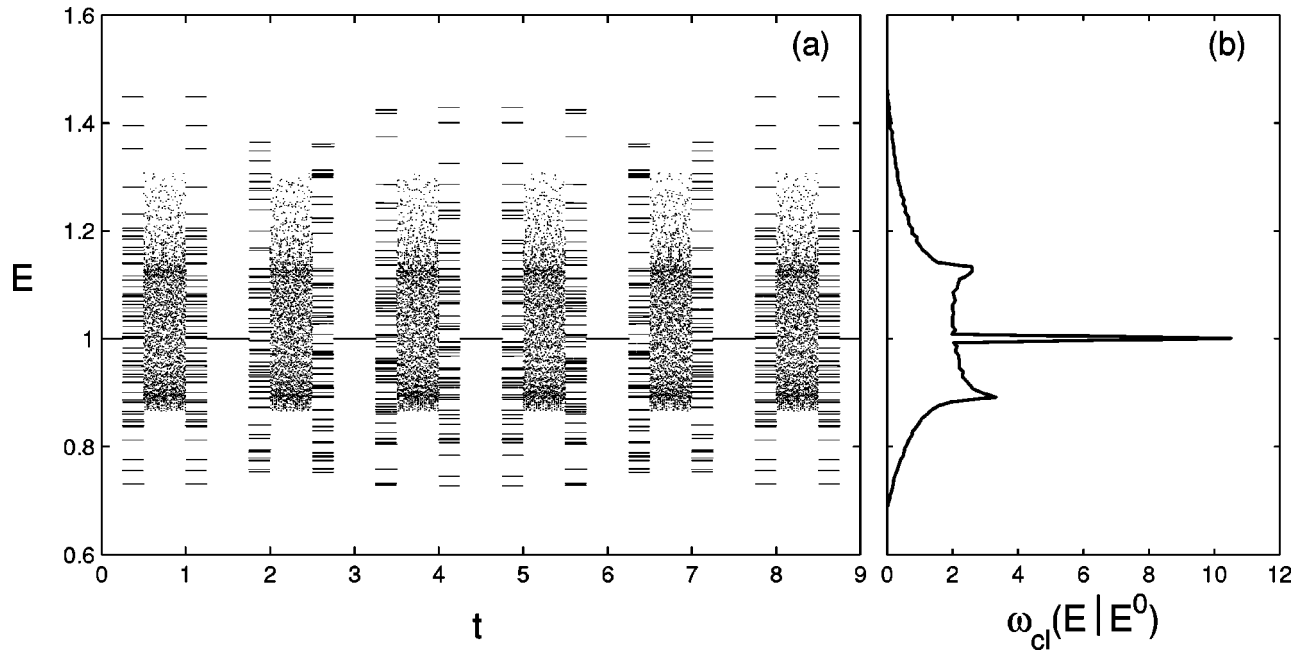

FIG. 9. (a) Energy $E(t)$ of the full Hamiltonian H as a function of time (in arbitrary units) after the substitution of 36 trajectories $\phi^0(t) \in H^0$ onto H for $E^0=1$. (b) Corresponding classical LDOS $\omega_{\rm cl}(E|E^0)$ constructed from $E(t)$. Note that each trajectory contributes in a different way to the classical distribution as can be seen in Fig. 9(a), for details see the text.

$=-\pi$). The initial conditions for the next sets are the same as for the first set, except u is shifted subsequently by $2\pi/5$. Any trajectory reveals one of these three types of behavior of $E(t)$; $E=1$, bar-code-like, and noiselike structure. The averaging over these time intervals yields the distribution shown in Fig. 9(b) quite different from the classical SES (Fig. 6) although it also has the central peak and two other peaks on each side.

VII. QUANTUM-CLASSICAL CORRESPONDENCE: GLOBAL PROPERTIES

Having understood the dynamical origin of the main features of the classical distributions $W_{\rm cl}(E^0|E)$ (SES) and $\omega_{\rm cl}(E|E^0)$ (LDOS), we now compare them with the corresponding quantum quantities. Although the SES for a given α, see Eq. (20), is actually the average over a set of perturbed states in the neighborhood of α, it is convenient, first, to examine typical *individual* states in different energy regions [31]. In order to compare the quantum and classical behavior, we use the quantum energy of interest E_q (where E_q is E^α in the case of SES and E_l^0 in the case of LDOS) to construct the classical distributions ($E_{\rm cl}=E_q$). The ratio of the de Broglie wavelength $\Lambda=2\pi\sqrt{\hbar^2/2m_eE}$ to some characteristic length of the billiard may be used as a semiclassical parameter (recall that there are two length parameters defining the flat channel, D and B; in this work we have used $D=B$). For example, $\Lambda/D=2\pi\hbar_{\rm eff}\ll 1$, where $\hbar_{\rm eff}\equiv\hbar/D\sqrt{2m_eE}$, tells us how large the energy of the eigenstate should be for its wavelength to be many times smaller than the width of the channel. Substitution of Weyl's formula $\overline{N}(E)=(BDm_e/2\pi\hbar^2)E$ into the above expression for Λ gives a more useful formula,

$$\Lambda/D=\sqrt{(B/D)(\pi/N)}=2\pi\hbar_{\rm eff}. \tag{22}$$

Here we only need to know the number of the eigenstate (as opposed to the energy) to determine the ratio Λ/D.

Figure 10 shows w_l^α for four representative states ($\alpha=111$, 712, 1362, and 2002) of different energy regions as a function of the unperturbed energy E_l^0 scaled to E^α. The classical SES is also shown. As it may be expected, these figures show that as $\hbar_{\rm eff}$ becomes smaller, the number of unperturbed states needed to form the perturbed state increases. Specifically, level states around $\alpha=111$ are still far from the semiclassical regime ($\Lambda/D\approx 0.17$); the details of the rippled boundary cannot be resolved and, thus, there is only a weak mixing of the unperturbed states. In contrast, for the state $\alpha=2002$ its de Broglie wavelength is a smaller fraction of the width of the channel ($\Lambda/D\approx 0.04$) and the number of participating components is larger.

It is important to note that although the number of unperturbed states needed to construct the perturbed state increases as the energy increases, they all fall within the range of energies determined by the classical distribution. This range defines the *energy shell* of the eigenstate under consideration. On the other hand, it is clear that even the level $\alpha=2002$ does not seem to have much of a resemblance with the classical distribution. For this and similar states, we have calculated the distribution of fluctuations around the classical curve and found that they deviate strongly from a Gaussian distribution as predicted by RMT considerations [31]. This may be related to the fact that the de Broglie wavelength of level 2002 is still not much smaller than the amplitude A of the ripple ($\Lambda/A\approx 0.66$, recall $A/D=0.06$). That is, even though Λ/D may be small, a more relevant parameter to characterize the semiclassical regime for particular eigen-

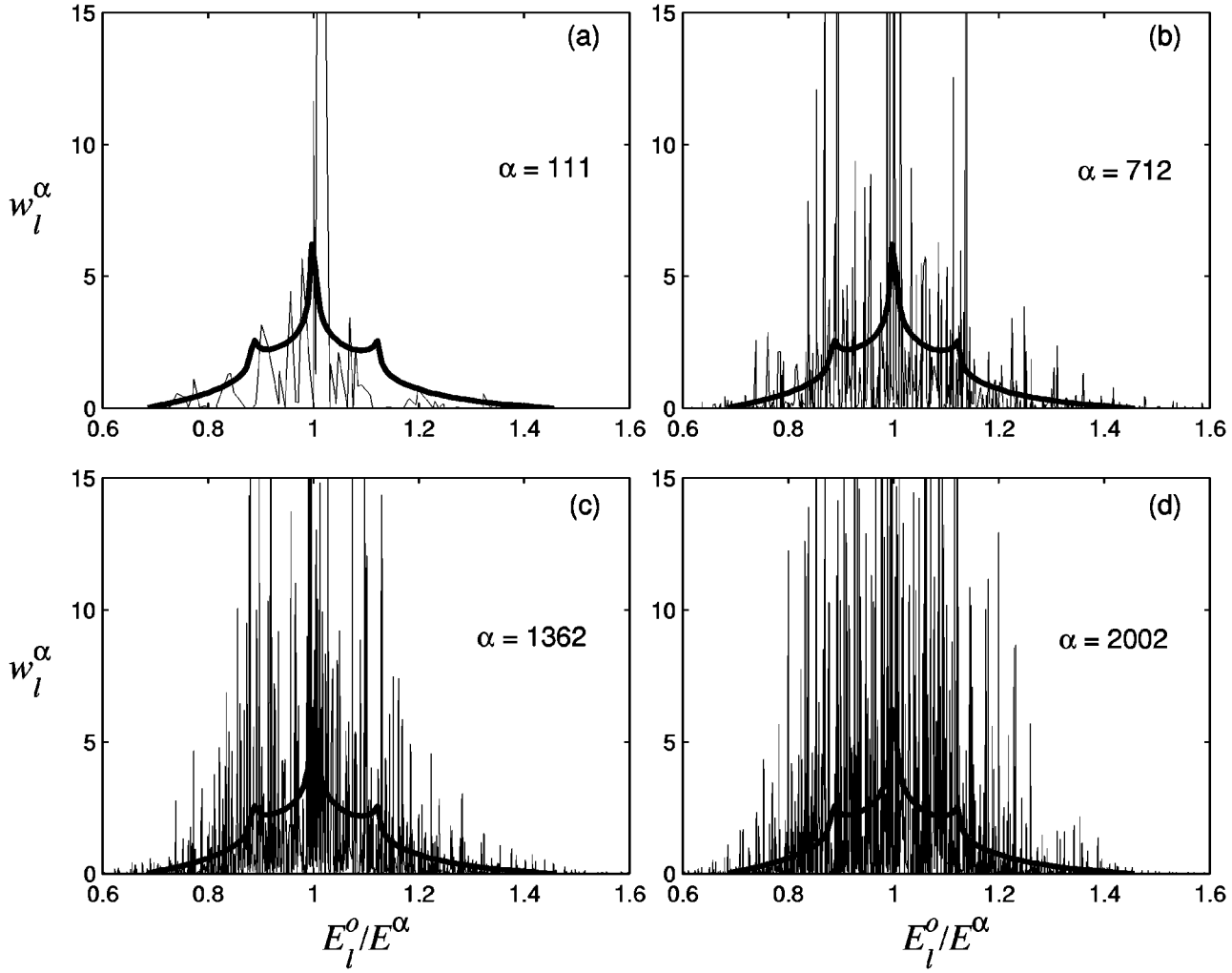

FIG. 10. Individual eigenfunctions w_l^α in the energy representation and the classical distribution $W_{\rm cl}(E^0|E)$ (thick curve) as a function of the energy E_l^0/E^α for $\alpha=$(a) 111, (b) 712, (c) 1362, and (d) 2002. The effective Planck constant $\hbar_{\rm eff}$ is (a) 0.027, (b) 0.011, (c) 0.008, and (d) 0.006, respectively. The entropy localization length (defined in Sec. VIII) $l_{\mathcal{H}}$ is (a) 23.6, (b) 158.9, (c) 483.6, and (d) 709.

states is Λ/A. Nevertheless the strong fluctuations exemplified by the level $\alpha=2002$ [Fig. 10(d)] can be smoothed out by averaging over a range of perturbed states. This actually corresponds to the definition (20) of the structure of eigenstates $W(E_l^0|E^\alpha)$.

Remarkably, as Fig. 11 shows, such an average does reveal a good quantum-classical correspondence even though the fluctuations are strong. Specifically, the global shape of the quantum SES displays a three-peak structure, much like the classical one. In addition, the energy spread of the quantum SES agrees very well with the classically determined energy shell, even in its slight asymmetry ($0.7<E^0<1.45$ with the center at $E^0=1$).

Similarly, in Fig. 12 we compare the quantum and classical LDOS. The quantum-classical correspondence appears to be even better than for the SES in the sense that the fluctuations are smaller.

VIII. LOCALIZATION AND NONERGODICITY

To understand the origin and importance of the strong fluctuations of the SES around the classical counterpart (see Fig. 11), we analyze the structure of *individual* eigenfunctions. In Fig. 13 three consecutive typical eigenfunctions ($\alpha=1952$, 1953, and 1954) are shown. The difference between the state $\alpha=1954$ and the other two is clearly qualitative. More specifically, while the states $\alpha=1952$ and 1953 are *extended* (in energy) states, constituted by practically all unperturbed eigenstates within the energy shell, the state $\alpha=1954$ is mostly unperturbed; it is extremely *localized* in the energy shell. By neglecting all small amplitude components surrounding the main component [see Fig. 13(c)], we can determine the unperturbed state, defined by a pair (m, n) that most closely resembles the perturbed state. We find that this always corresponds to the lowest values of the transversal mode m. This fact can be understood by the following physical argument. Consider an eigenstate of the flat channel $\phi^0_{m,n}(X,Y)\propto\sin(m\pi Y/D)\exp(iKX)$ with energy $E^0=(\hbar^2/2m_e)(K_x^2+K_y^2)$, where $K_y=m\pi/D=2\pi/\Lambda_y$. Turning on the perturbation (flat to rippled channel) will affect the high energy unperturbed states differently depending mainly on the value of Λ_y. For example, for $m=1$, the ratio Λ_y/A is

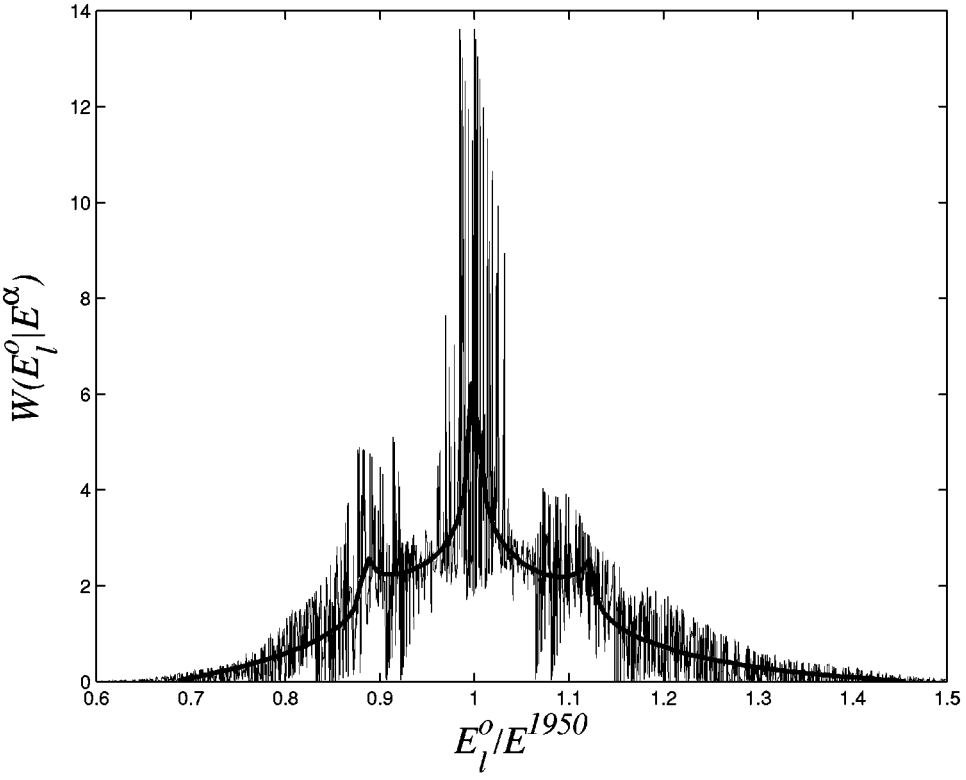

FIG. 11. Structure of eigenstates (SES) in the energy representation $W(E_l^0|E^\alpha)$ and its classical counterpart $W_{\rm cl}(E^0|E)$ (thick curve). The average for the SES is taken over the interval $1880<\alpha<2025$.

$2D/A\approx 33$, which is so large that the state cannot ''see'' the ripple and thus will remain essentially unperturbed. In contrast, for unperturbed states with the same (or about the same) energy but with large values of m (say, $m=62=M_{\rm max}$ and correspondingly small k_x) their Λ_y is sufficiently small, compared to the amplitude of the ripple ($\Lambda_y/A\approx 0.5$), that the rippled boundary produces a strong mixing of unperturbed levels. The resulting perturbed state will consist of many components, extended over the energy shell. By the same token, it is expected that unperturbed states with intermediate values of m will turn, after turning on the perturbation, into some intermediate states, the so-called sparse

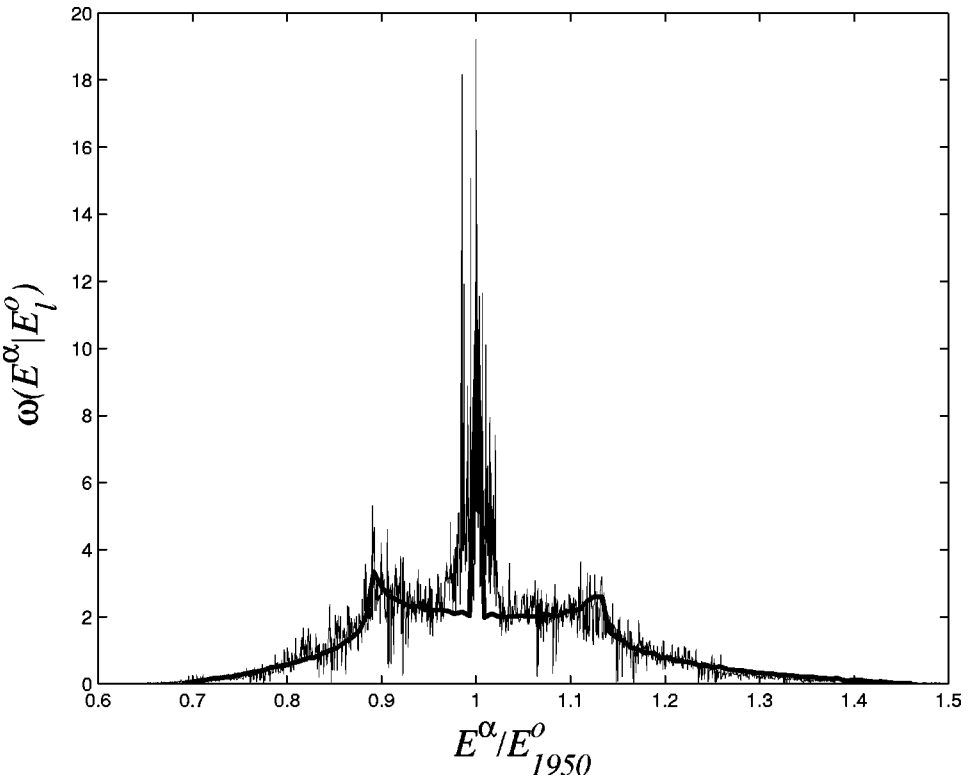

FIG. 12. LDOS $\omega(E^\alpha|E_l^0)$ and its classical counterpart $\omega_{\rm cl}(E|E^0)$ (thick curve). For the LDOS the average is taken over the interval $1900<l<2000$.

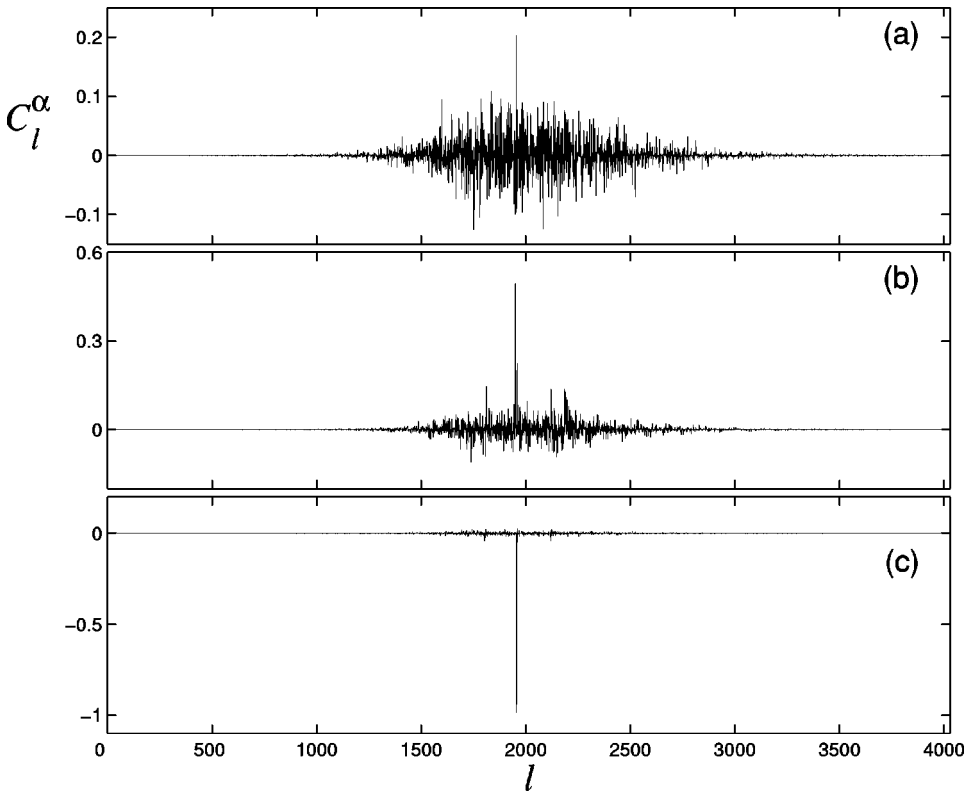

FIG. 13. Typical high energy eigenfunctions for (a) $\alpha=1952$, (b) $\alpha=1953$, and (c) $\alpha=1954$. The localization measures (defined below) are (a) $l_H=745.9$, $l_{\mathrm{ipr}}=529.7$; (b) $l_H=232.9$, $l_{\mathrm{ipr}}=45.4$; and (c) $l_H=2.7$, $l_{\mathrm{ipr}}=3.2$.

states [32], made up of fewer components over the energy shell.

The existence of the extremely localized (in energy) states manifests itself in the structure of the Hamiltonian matrix $H_{l,l'}$ in the channel representation (Fig. 2) to be discussed below. It is easy to find that such wave functions differ only slightly from the plane waves $\phi^0_{m,n}(x,y)$ with small m, proper of the flat channel. In Fig. 14(a) one localized (in energy) state is shown in configuration representation. In contrast, an extended (in energy) state is presented in Fig. 14(b).

Eigenfunctions like that of Fig. 13(b) for $\alpha=1953$ are somewhat intermediate between the extended and localized states.

In order to characterize quantitatively the eigenfunctions, we compute various localization measures. The first one is the so-called *entropy localization length* l_H,

$$l_H=\exp[-(\mathcal{H}-\mathcal{H}_{\mathrm{GOE}})]\approx 2.08\exp(-\mathcal{H}). \tag{23}$$

Here $\mathcal{H}$ stands for the Shannon entropy of an eigenstate in a given basis,

$$\mathcal{H}=\sum_{i=1}^{N} w_l^\alpha \ln w_l^\alpha, \tag{24}$$

and $\mathcal{H}_{\mathrm{GOE}}$ is the entropy of a completely chaotic state, which is characterized by Gaussian fluctuations (for $N\to\infty$) of all components C_l^α with the same variance $\langle w_l^\alpha\rangle=1/N$. The latter property occurs for completely random matrices belonging to a Gaussian orthogonal ensemble (GOE). Defined in this way, the quantity l_H gives a measure of the effective number of components in an eigenstate. For example, the eigenstates of Fig. 13 have, respectively, $l_{\mathcal{H}}=745.9$, 232.9, and 2.7.

The second quantity l_{ipr}, which gives another measure of the effective number of components in an eigenstate, is expressed via the *inverse participation ratio* $\mathcal{P}$,

$$l_{\mathrm{ipr}}=\left[\frac{\mathcal{P}_{\mathrm{GOE}}}{\mathcal{P}}\right]\approx\frac{3}{\mathcal{P}} \tag{25}$$

with

$$\mathcal{P}=\sum_{l=1}^{N}(w_l^\alpha)^2 \tag{26}$$

where $\mathcal{P}_{\mathrm{GOE}}\approx 3$ is chosen in order to get $l_{\mathrm{ipr}}=N$ in the GOE-limit case.

The above two definitions of ''localization lengths'' are the most frequently used when describing global structure of eigenfunctions. One should note that these quantities give an effective number of large components, independently on the location of these components in the unperturbed basis.

Additional information about the structure of eigenfunctions can be obtained from the ''width'' or mean square root l_σ of an eigenstate, computed as

$$l_\sigma=\left\{\sum_{l=1}^{N} w_l^\alpha[l-n_c(\alpha)]^2\right\}^{1/2} \tag{27}$$

where $n_c=\Sigma_l l w_l^\alpha$ determines the centroid of an eigenstate in the unperturbed basis.

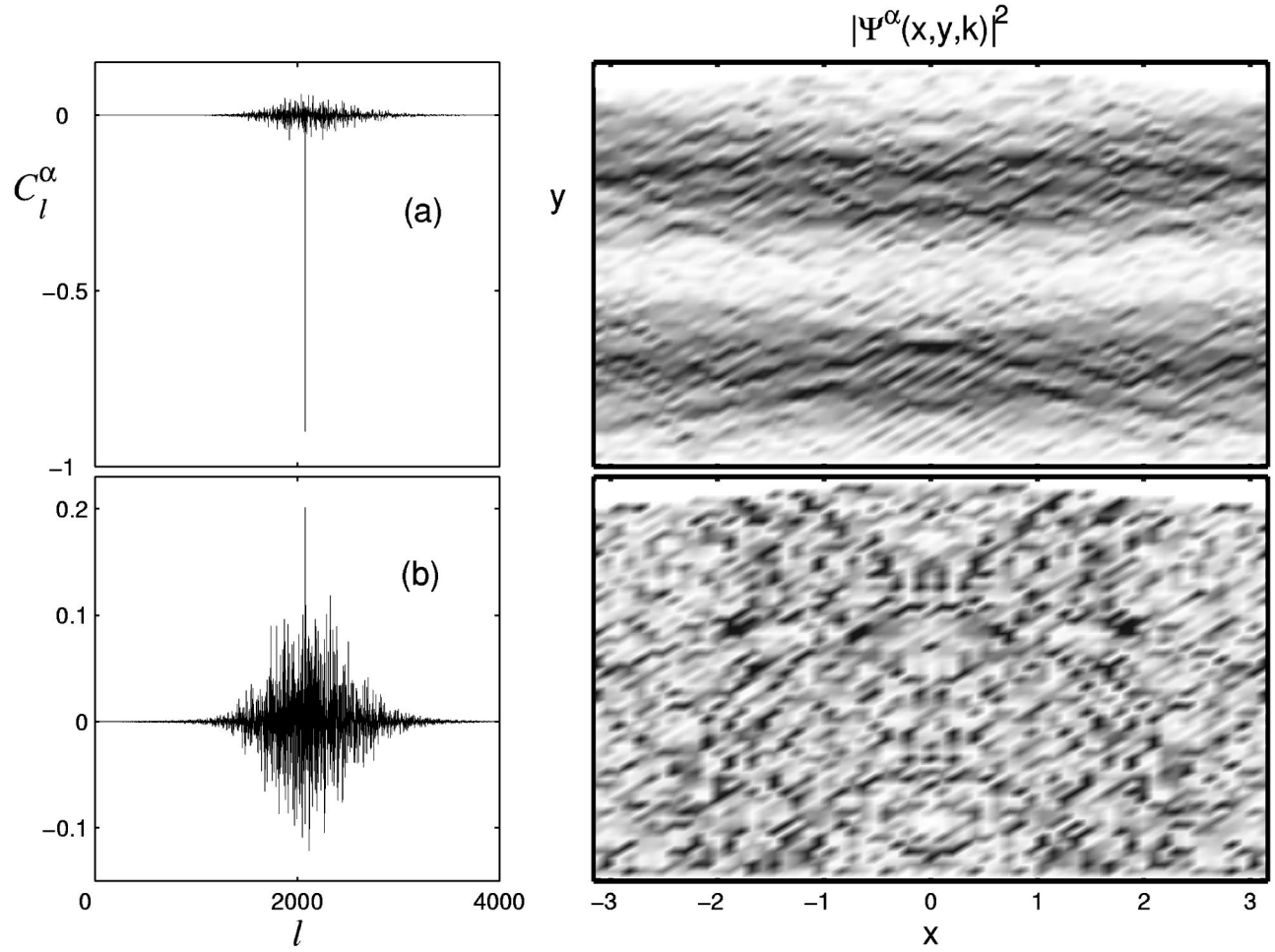

FIG. 14. Left: A localized and an extended eigenfunction in the basis representation for (a) $\alpha=2082$ (extremely localized state with corresponding $m=2$), (b) $\alpha=2083$. Right: The same eigenfunctions in configuration representations.

To get a complete panorama, in Figs. 15(a)–15(c) we plot these three measures as a function of α corresponding to the eigenstate $|\alpha\rangle$. The strong fluctuations of all localization measures are evident in these figures. We can see that neighboring high levels may have drastically different localization measures, in agreement with the discussion above about the existence of the three types of states: localized, extended, and sparse. These figures give us information about the relative number of each type to be found in a given energy range.

Comparison of the width l_σ with l_H and l_{ipr} gives the possibility to detect the so-called *sparsity* of eigenstates. Indeed, small values of the ratio l_H/l_σ (or $l_{\mathrm{ipr}}/l_\sigma$) indicate that there are many ''holes'' in the structure of eigenstates, therefore, such eigenstates are *sparse* [32]. A detailed analysis shows a dominance of sparsed eigenstates. As for the centroid $n_c=\alpha$, small fluctuations [observed in Fig. 15(c)] indicate that the interaction strength V is relatively weak, compared to the unperturbed part H_0.

The data of Fig. 15 show the existence of some pattern for all localization measures, visible as clusters of points in the lower part of the plots. These patterns are much more pronounced for the same quantities computed for the LDOS, see Fig. 16. In order to understand this unexpected phenomenon, let us take a closer look at l_σ in the range $1450<l<2100$ and examine the structure shown in Fig. 17 in detail. Specifically, we choose some eigenstates from three branches of points (see marked states in Fig. 17). From each of these three sets, we take the 1st, 7th, 13th, and 19th states counted from the bottom of the figure and plot them in Fig. 18. Inspection of Figs. 18(a)–18(c) clearly demonstrates that there is a kind of regularity in the structure of the LDOS: the same type of states appear repeatedly, almost periodically as a function of the basis number l. These figures show the repetition of extremely localized states [Fig. 18(a)] and of states with different degrees of sparsity [Figs. 18(b)–18(d)]. The repetition of extended states, corresponding to larger vaues of l_σ are not shown for economy of space but their existence is clear, as can be inferred by extrapolating the branches of Fig. 17 to higher values of l_σ. The physical origin of all these types of states (localized, sparse, and extended) was explained above, and their appearance can be decoded by examining the structure of the ''channel representation'' of the Hamiltonian matrix (Fig. 2). A detailed inspection of this matrix [see also Eq. (26) of Ref. [10]] shows that the coupling between unperturbed states depends strongly on the values of the index m, labeling the transversal modes of the flat billiard. An unperturbed state specified by a large value of m (an m close to

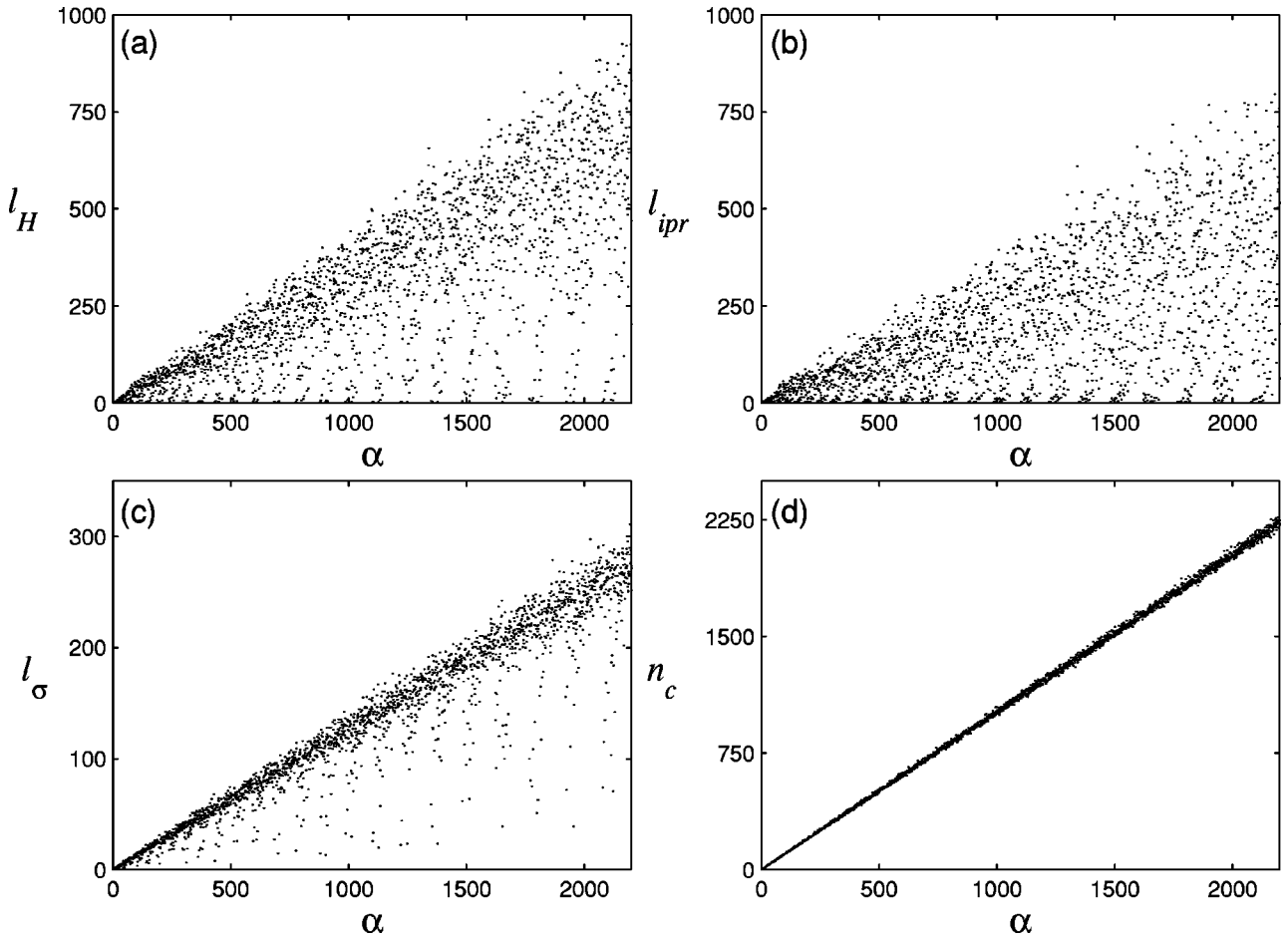

FIG. 15. Localization measures for eigenfunctions dependent on α for exact αth eigenstates. (a) Entropy localization length $l_{\mathcal{H}}$, (b) l_{ipr} defined through the inverse participation ratio, (c) the mean square root l_σ, and (d) the centroid n_c.

$M_{\max}=62$) couples strongly to several other unperturbed states. In contrast, a state with $m=1$ has practically no coupling to other states. In particular, the extremely localized states, corresponding to the first position on the left line of each branch of Fig. 17, occur because of the negligible coupling of the diagonal elements of the $H_{l,l'}$ matrix with $m=1$, the states on the second position of each branch occur for $m=3$, and so on with m odd. Similarly, states on the right side of the branches result from elements of the $H_{l,l'}$ matrix with even values of m.

This structure is expected to prevail at all energy ranges since in any sufficiently large range of energies there are unperturbed states with all values of m in $[1,M_{\max}]$. Even deep in the semiclassical regime, extremely localized and sparse states will appear but less and less frequently since the energy differences between states of the same type increase with energy. Consequently, the strong fluctuations appearing in the SES and LDOS distributions (Figs. 11 and 12) will tend to disappear as $\hbar_{\mathrm{eff}}\to 0$.

In the definitions of SES and LDOS, the averages were performed over the appropriate range of energy in order to take into account once all the various types of states (Figs. 10 and 11 were calculated this way).

We can understand the origin of this type of regular structure by analyzing the Hamiltonian matrix $H_{l,l'}$, see Fig. 2. A detailed inspection shows that for the unperturbed states (diagonal matrix elements), the coupling with other unperturbed states depends on the value of the index m, which labels the number of transversal modes in the billiard [see Eqs. (11) and (12)]. An unperturbed state specified by a large m (an m close to $M_{\max}=62$, for any n) shows a strong coupling to several other unperturbed states. In contrast, a state with $m=1$ (for any n) shows practically no coupling to other states.

We can see then that the extremely localized states, corresponding to the first position on the left-hand side of each set of points in Fig. 16, occur because of the negligible coupling of the diagonal elements of the $H_{l,l'}$ matrix with $m=1$. Similarly, the states on the second position (on the left-hand side) occur when $m=3$, and so on with odd m. States on the right-hand side of each set of points result from elements of the $H_{l,l'}$ matrix with even values of m. This structure prevails for all energies due to the existence of unperturbed $m=1$ states. However, the intervals between the occurrence of $m=1$ unperturbed states increase as the energy increases. Even as the semiclassical limit is approached, extremely localized states will appear, except that they will be less and less frequent. Consequently the strong fluctuations appearing in the SES and LDOS distributions (Figs. 10 and 11) will tend to disappear.

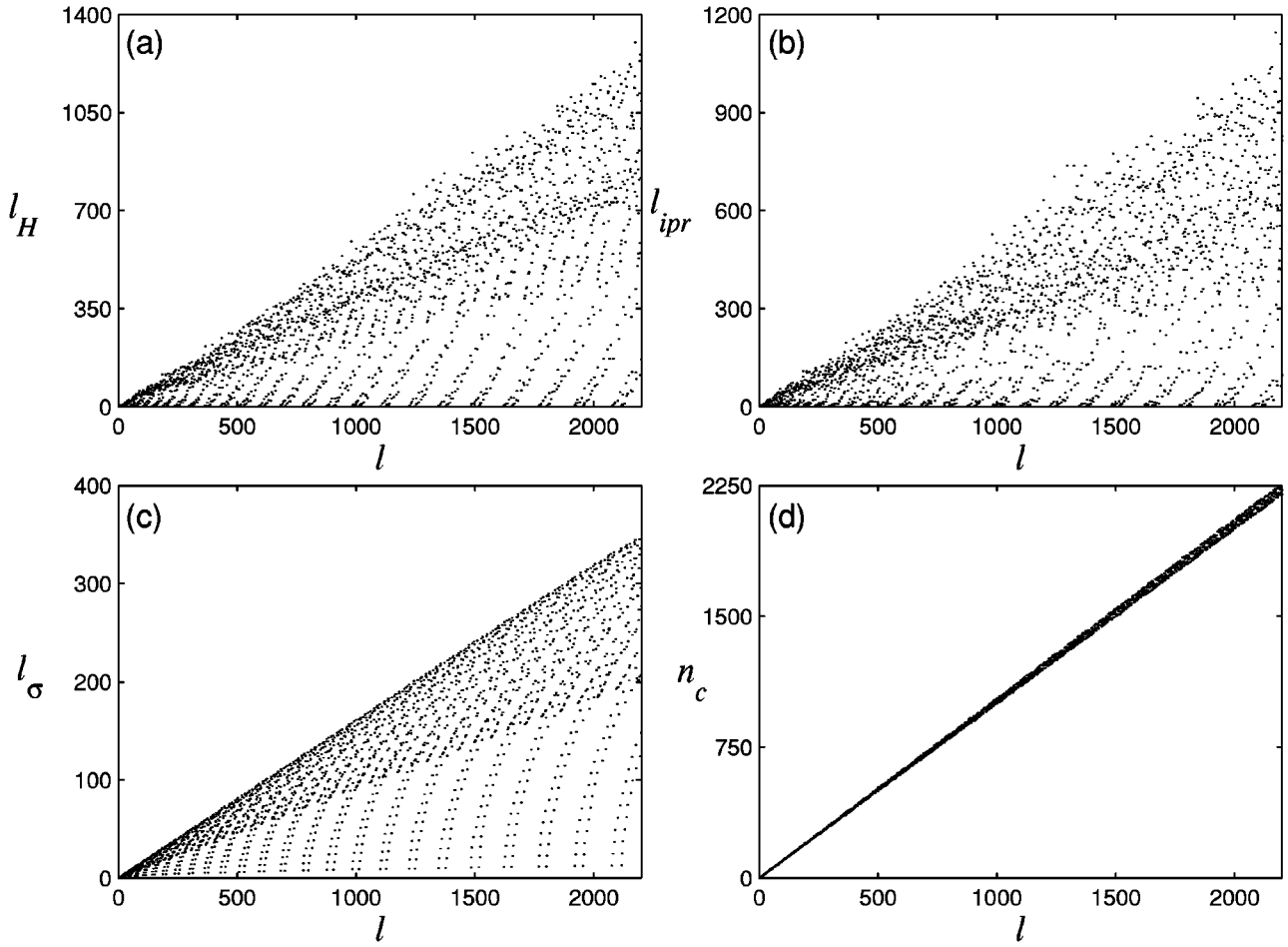

FIG. 16. Localization measures for the LDOS with l standing for the unperturbed state $|l\rangle$. Same localization measures as in Fig. 15 are presented: (a) $l_{\mathcal{H}}$, (b) l_{ipr}, (c) l_σ, and (d) n_c.

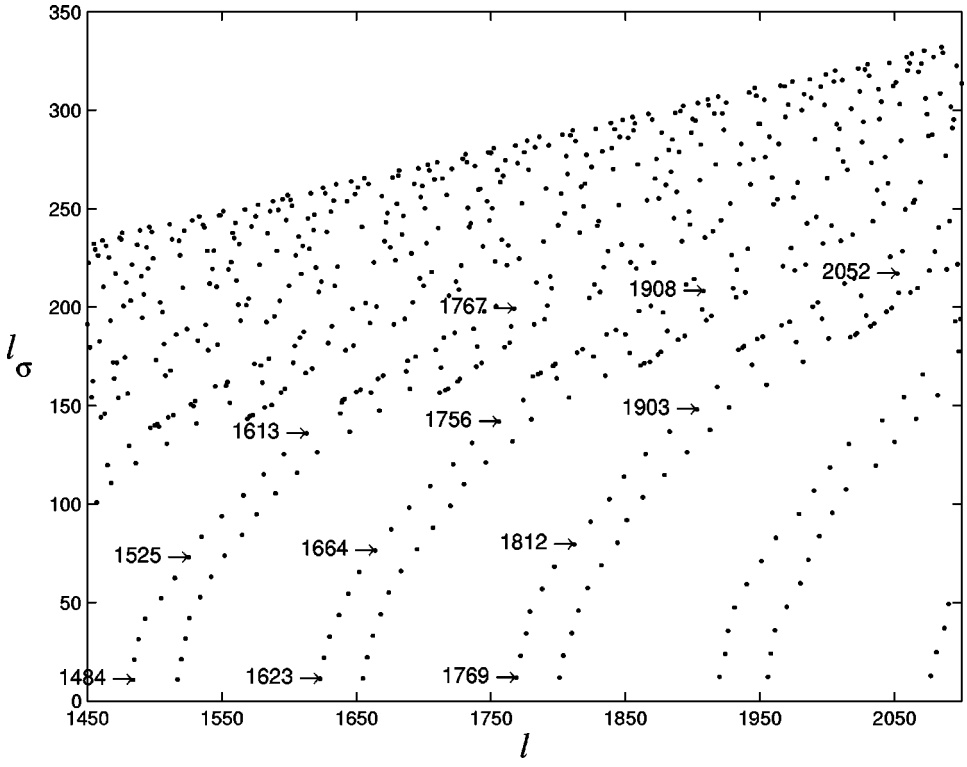

FIG. 17. Detail of Fig. 16(c) for the range $1450<l<2100$. The numbers indicate specific states that are shown in Fig. 18. The states are chosen from three different sets of states, specified by almost the same values of l_σ.

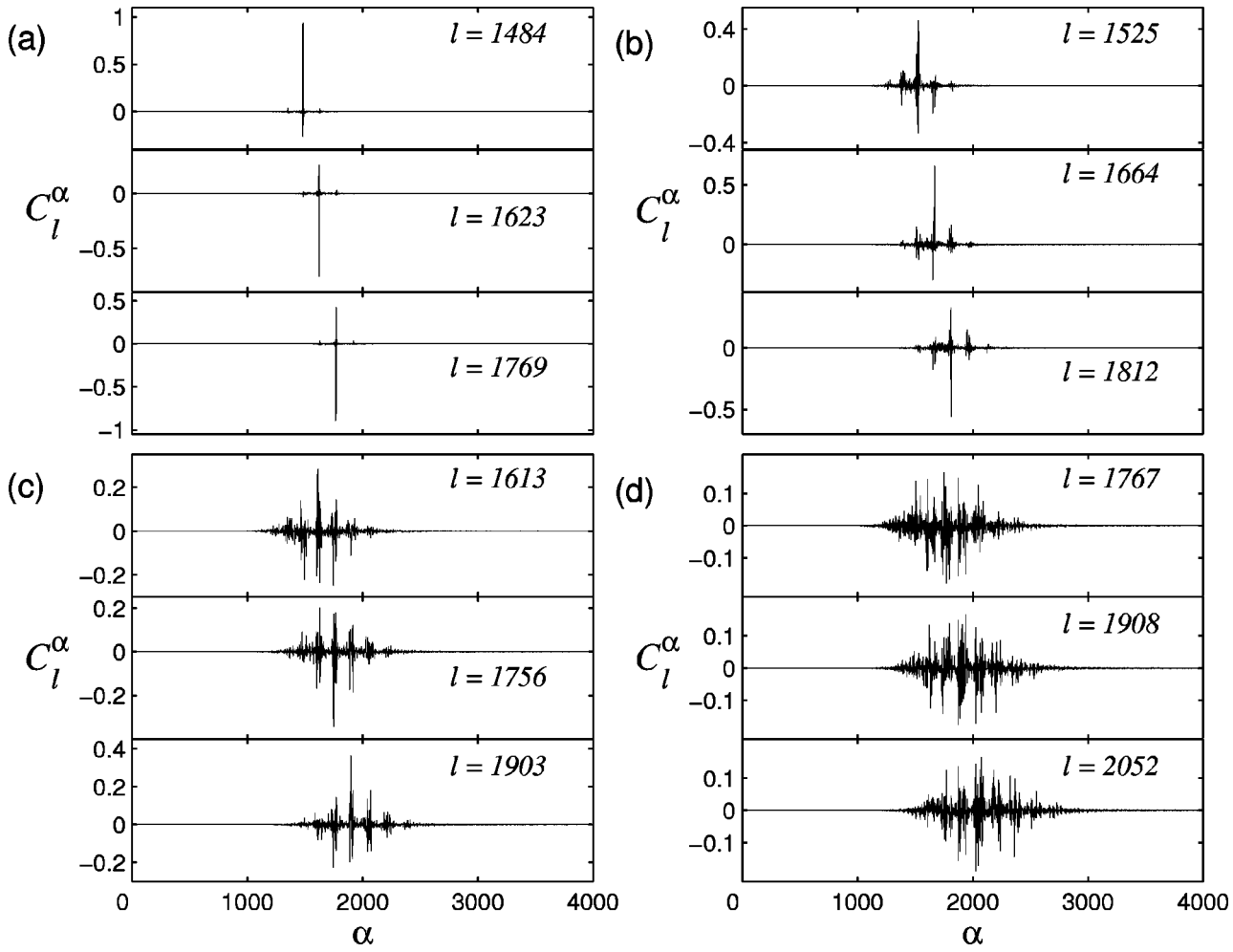

FIG. 18. Structure of individual LDOS marked in Fig. 17. One can see the similarity in the structure of the LDOS taken from different sets, but with the same values of l_σ.

IX. CONCLUDING REMARKS

The quantum-classical correspondence for the chaotic motion of an electron in a periodic billiard was analyzed in terms of the classical analog of the SES and LDOS.

To construct the classical counterparts of the LDOS and SES, we first changed (via a canonical transformation) to some new curvilinear coordinates, where the new Hamiltonian incorporated the effects of the boundary into an effective interaction potential. Then the original system of a free particle colliding within a 2D rippled channel becomes equivalent to a 1D model of two interacting ''particles,'' identified with the new coordinates. This procedure allowed us to study the chaotic properties of this system using tools developed recently to analyze the role that interactions between particles play in the onset of quantum chaos. This example is quite instructive since it shows the connection between ''one-body chaos,'' which is due to an external potential (or boundary conditions), and ''two-body chaos,'' which results entirely from the interaction between particles. So far, these two mechanisms for producing chaos have been treated completely independently.

Using this approach, we found that in the case of strong chaos, the classical analogs of SES and LDOS agreed remarkably well with the global shapes of the quantum quantities. This correspondence enabled us to explain the main features of the SES and LDOS in terms of the underlying classical motion of the system. Specifically, we found that classical unstable and stable periodic orbits of period 1 give rise to the two pronounced side-band peaks observed in the SES and LDOS.

On the other hand, we found that the statistical properties of eigenstates and individual LDOS differ qualitatively from those prescribed by the standard random matrix theory. Namely, in the case of strong chaos and deep in the semiclassical region (high energy), one expects the components of individual eigenstates to fluctuate in a statistically independent way around the mean, the envelope of the SES in the unperturbed energy basis. This expectation was confirmed when studying the structure of eigenstates of complex atoms and nuclei in the mean-field basis [34,35]. In contrast, we have found that in our present model the deviations turn out to be extremely strong and not fully statistically independent.

In connection with this, a detailed analysis revealed quite unexpected regularities in localization measures (such as the inverse participation ratio) characterizing the eigenstates and

individual LDOS. We remark that these regularities do not disappear as energy increases. In particular, even for high energies, one can find eigenstates that are strongly localized in the unperturbed energy representation (i.e., slightly perturbed plane waves). This occurs because energy is not the only semiclassical parameter in a 2D electron waveguide. Clearly, two unperturbed states of similar (or equal) energy values but different transverse mode numbers will react differently to a small perturbation. That is, in contrast to high-mode unperturbed states, the transverse wavelength Λ_y for low-mode states can be many times larger than the amplitude of the perturbation and hence will remain essentially unperturbed.

Thus, for any value of energy (equivalently, for any small value of $\hbar$), there are *non-ergodic states*. It should be stressed that here we are discussing the ergodicity in the energy shell, which is determined by the classical motion of a particle in terms of the classical SES. Since the width of the energy shell is always finite due to the finite range of the interaction, the ergodicity of an eigenstate means that this eigenstate fills the whole energy shell with random (Gaussian) fluctuations of its components around the smooth energy dependence defined by the classical SES.

Naturally, with an increase of the energy, the *relative* number of localized (in the energy shell) eigenstates tends to zero. In this sense, there is no contradiction with the onset of quantum ergodicity in the classical limit. However, this limit turns out to be achieved very slowly. Therefore, we remark that from a physical point of view, it is important to further the study of the statistical properties of eigenstates in the deep semiclassical regime, which may be different from those in the strictly classical limit ($\hbar=0$, a mathematical concept).

ACKNOWLEDGMENT

We acknowledge support from CONACyT (Mexico) through Grant No. 26163-E.

[1] F. Borgonovi, I. Guarneri, and F. M. Izrailev, Phys. Rev. E **57**, 5291 (1998).

[2] L. Benet, F. M. Izrailev, T. H. Seligman, and A. Suárez-Moreno, Phys. Lett. A **277**, 87 (2000).

[3] L. Meza-Montes, F. M. Izrailev, and S. E. Ulloa, Phys. Status Solidi B **220**, 721 (2000).

[4] Weng-ge Wang, F. M. Izrailev, and G. Casati, Phys. Rev. E **57**, 323 (1998).

[5] G. A. Luna-Acosta, J. A. Méndez-Bermúrdez, and F. M. Izrailev, Phys. Lett. A **274**, 192 (2000).

[6] J. L. Tennyson, AIP Conf. Proc. **57**, 158 (1979).

[7] A. J. Lichtenberg and M. A. Lieberman, *Regular and Chaotic Dynamics*, 2nd ed. (Springer-Verlag, New York, 1992), Sec. 6.1b.

[8] G. A. Luna-Acosta, A. A. Krokhin, M. A. Rodriguez, and P. H. Hernandez-Tejeda, Phys. Rev. B **54**, 11 410 (1996).

[9] B. Huckestein, R. Ketzmerick, and C. H. Lewenkopf, Phys. Rev. Lett. **84**, 5504 (2000); Gursoy B. Akguk and L. E. Reichl, J. Stat. Phys. **98**, 813 (2000).

[10] G. A. Luna-Acosta, K. Na, L. E. Reichl, and A. Krokhin, Phys. Rev. E **53**, 3271 (1996).

[11] E. R. Mucciolo, R. B. Capaz, B. L. Altshuler, and J. D. Joannopoulos, Phys. Rev. B **50**, 8245 (1994).

[12] T. Dittrich, B. Mehlig, H. Schanz, and U. Smilansky, Phys. Rev. E **57**, 359 (1998).

[13] C. S. Lent and M. Leng, J. Appl. Phys. **70**, 3157 (1991).

[14] V. Ya. Demikhovskii, S. Yu. Potapenko, and A. M. Satanin, Fiz. Tekh. Poluprovodn. **17**, 213 (1983) [Sov. Phys. Semicond. **17**, 137 (1983)].

[15] W-D. Sheng and J. B. Xai, J. Phys.: Condens. Matter **8**, 3635 (1996).

[16] E. Vergini and M. Saraceno, Phys. Rev. E **52**, 2204 (1995).

[17] In Ref. [10], a slightly different transformation was used. There $v \equiv y/[d+a\cos(x)]$, which contains the two parameters a and b but the wave function vanishes at $y=1$.

[18] R. Adler, M. Bazin, and M. Schiffer, *Introduction to General Relativity* (McGraw-Hill, New York, 1975).

[19] B. Dewitt, Rev. Mod. Phys. **29**, 377 (1957).

[20] V. V. Flambaum and F. M. Izrailev, Phys. Rev. E **56**, 5144 (1997).

[21] See, e.g., R. L. Ingraham, *A Survey of Nonlinear Dynamics: Chaos Theory* (World Scientific, Singapore, 1992), Sec. 7.4.

[22] G. A. Luna-Acosta, M. A. Rodriguez, A. A. Krokhin, K. Na, and R. A. Méndez, Rev. Mex. Fis. **44**, 7 (1998).

[23] G. Casati, F. Valz-Gris, and I. Guarneri, Lett. Nuovo Cimento Soc. Ital. Fis. **28**, 279 (1980); O. Bohigas, M. J. Giannoni, and C. Schmit, Phys. Rev. Lett. **52**, 1 (1984).

[24] Weyl's formula gives $\overline{E} \equiv E/E^* = 4\langle N(\overline{E})\rangle/\pi(D/B)$, where the area S equals BD for the cosine profile as well as for the flat channel; B is the period and D the width (in our calculations here we use $B=D$). Then we equate the average $\langle N(\overline{E})\rangle$ with the energy-ordered level l.

[25] V. V. Flambaum and F. M. Izrailev, Phys. Rev. E **61**, 2539 (2000).

[26] F. M. Izrailev, in *New Directions in Quantum Chaos, Proceedings of the International School of Physics "Enrico Fermi," Course CXLIII, Varenna*, edited by G. Casati, I. Guarneri, and U. Smilansky (IOS Press, 2000), pp. 371–430.

[27] The approximation consists in assuming that the particle collisions with the top boundary take place always at $y=d$ but that the direction of reflection is given by the slope of the ripple at x_n.

[28] It is interesting to note that (through the use of commutation relations, like $[\hat{P}_\alpha, g^{-1/4}] = -i\hbar\partial_\alpha g^{-1/4}$), the quantum Hamiltonian (8) becomes $H = \frac{1}{2} P_\alpha g^{\alpha\beta} P_\beta + \hbar^2 Q(u,v)$, where $Q(u,v) = (\epsilon/4)(\xi_{uu}/g^{1/2} - 3\epsilon\xi_u^2/g)$. By comparison with the classical Hamiltonian (17), the quantity Q may be interpreted (see, e.g., [33]), as a sort of quantum potential that must be added to the covariant classical expression in order to produce the correct quantum covariant Hamiltonian.

[29] G. Casati, B. Chirikov, I. Guarneri, and F. M. Izrailev, Phys. Lett. A **223**, 430 (1996).
[30] F. Borgonovi, I. Guarneri, F. M. Izrailev, and G. Casati, Phys. Lett. A **247**, 140 (1998).
[31] F. Borgonovi, I. Guarneri, and F. M. Izrailev, Phys. Rev. E **57**, 5291 (1998).
[32] T. Prozen and M. Robnik, J. Phys. A **25**, 1105 (1993).
[33] B. S. DeWitt, Phys. Rev. **85**, 653 (1952).
[34] V. V. Flambaum, A. A. Gribakina, G. F. Gribakin, and M. G. Kozlov, Phys. Rev. A **50**, 267 (1994).
[35] V. Zelevinsky, B. A. Brown, M. Horoi, and N. Frazier, Phys. Rep. **276**, 85 (1996).